NUMERICAL EVALUATION OF THE HEAT TRANSFER PERFORMANCE OF WATER-COOLED SYSTEM FOR ELECTRIC VEHICLE DRIVE MOTOR BASED ON THE FIELD SYNERGY PRINCIPLE

by

Jiacheng ZHANG[a], Jiaming ZHANG[b*], and Zining LIU[c]

[a]School of Electrical and Electronic Engineering, Harbin University of Science and Technology, Harbin, China
[b]Jinchuan Yangjiawan Water and Power Co., Ltd, Chengdu, China
[c]Dongfang Electronics Co., Ltd, Yantai, China

Original scientific paper
https://doi.org/10.2298/TSCI230422164Z

Thermal management of drive motors is a challenging design for transport electrification industries such as electric vehicles. Due to the high heat transfer performance, water-cooled system have become one of the technologies to meet the needs of these industries. Meeting the synergy between the heat transfer performance of the water-cooled system and the heat generated by the motor is key to taking advantage of the performance of drive motors. This study numerically evaluates and experimentally investigates the heat transfer performance of the electric vehicles drive motor water-cooled system based on field synergy principle, discussing the synergy between the temperature gradient field and velocity field of the water-cooled system under different cooling conditions, and the calculated results are consistent with the test results. By observing the interaction between the fluid vortexes and the main flow, the distribution pattern of the synergy angle in the cooling channels was determined. The results show that when the heat transfer capacity of the water-cooled system reaches its peak, the increase in Reynolds number instead leads to the increase in the average synergy angle of the whole field, which ultimately causes a deterioration of synergy between the velocity and temperature gradient fields.

Key words*: field synergy principle, thermal management, drive motors, water-cooled system, heat transfer performance*

Introduction

The accelerated depletion of non-renewable resources, represented by fossil energy, has driven us to constantly search for new clean energy sources [1-3]. In this background, the electric vehicles (EV) industry has achieved rapid development [4]. With the continuous progress in the production and development of EV, the technical route of replacing the internal combustion engine by electric motors has become clearer. This replacement not only significantly reduces GHG emissions, but also effectively saves fossil fuel consumption [5, 6]. At present, permanent magnet synchronous motors (PMSM) are widely recognized and used in the

*Corresponding author, e-mail: crow_n@foxmail.com

electric vehicle industry for their favorable speed range, excellent NVH performance, and beneficial economics [7-9]. Compared with other industrial motors, PMSM as EV drive motors not only need to face frequent changes in daily operating conditions (*e.g.*, hill climbing and acceleration states), but also the development of PMSM toward high power density and light weight have challenged the heat transfer performance of the motors [10, 11]. All of the aforementioned factors will further exacerbate the temperature increase inside the motor, and the high temperature will eventually lead to abnormal aging of the stator insulation material. Worse still, the high temperature will cause irreversible demagnetization of the permanent magnets, which will seriously affect the safety and service life of the PMSM [12]. Therefore, it is essential to investigate the heat transfer mechanism of the PMSM water-cooled system, to provide an effective cooling system for the motor, and to ensure the stability and service life of the motor operation.

The cooling of EV drive motors is mainly dependent on convection heat transfer from the water-cooled system, which is currently the most widespread application solution. The heat transfer performance of water-cooled motors is not only related to the losses in the motor, but also to the cooling channels and various structural parameters of the water-cooled system. Petrov *et al*. [13] compared the winding direct oil-cooled scheme with the spiral water-cooled scheme in detail, and determined the effect of the cooling system on the output torque and output power of PMSM. In order to investigate the relationship between water-cooled structural parameters and thermal characteristics of high-speed permanent magnet motors, Du *et al*. [14] determined the relationship between the thermal characteristics of HSPMM rotors and factors such as cooling channels thickness through electro-magnetic-thermal iterative calculations. Chang *et al*. [15] proposed a new water-cooled system for axial flux permanent magnet motors, using the FEM to numerically calculate the temperature field of the AFPMM, and increased the peak motor power by 30% while the experimental data matched well with the numerical results. Gai *et al*. [16] to improve the heat dissipation performance of PMSM in weakly magnetically controlled operation, developed a simplified temperature field model that accurately evaluates the relationship between speed, fluid-flow velocity and stator temperature, reducing the complexity of modelling hybrid cooling system. Lindh *et al*. [17] designed a hybrid cooling system combining water cooled with winding oil-cooled in order to improve the thermal management of drive motors, and determined the feasibility of hybrid cooling system in the thermal management of PMSM, especially when stator copper losses account for a relatively large share.

Notably, in the study on fluid heat transfer, Guo *et al*. [18-20] provided new insights into the physical mechanism of convective heat transfer, namely the field synergy principle (FSP). By establishing the synergy equation based on the conservation of thermal energy, they determined that the synergy between the temperature gradient field and the velocity field can elucidate the physical mechanism of convective heat transfer. In other words, under the same velocity and temperature boundary conditions, the synergy between the velocity and temperature gradient fields shows a positive correlation with the heat transfer intensity [21]. Authors in [22-24] demonstrated the accuracy and effectiveness of the FSP through various experiments on incompressible fluids and provided a detailed exposition of the process. To further develop FSP, Liu *et al*. [25, 26] proposed the concept of laminar flow field synergy, revealing the relationship between the synergy angle and laminar flow resistance, providing guidance for the design of efficient heat exchangers. Fu *et al*. [27] applied FSP to the study of convective heat transfer in air-cooled motor and determined the difference between FSP in the stationary and rotating coordinate systems. In the literature, FSP is considered to be the guiding principle

regarding fluid heat transfer. However, there is a blank space in the application of FSP in the field of water-cooled PMSM. Furthermore, with the update and iteration of EV drive motor cooling technology, the water-cooled systems for PMSM have become more complex.

Based on the aforementioned, an EV drive motor with an axial water-cooled system was built. The FEM was used to calculate the temperature distribution of the motor and the heat transfer characteristics of the fluid, and to analyze the synergy between the temperature gradient field and the velocity field of the drive motor under different cooling conditions, including the distribution pattern of the cosine of the synergy angle with changing Reynolds number, and the influence of the structural parameters of the water-cooled system on the field synergy number, *Fc*. In addition, a drive motor water cooling test platform was built and the numerical results were compared with the test results. We believe that the results of the study can provide new ideas for improving the thermal management of EV drive motors, and supply research data and application value for the field synergy evaluation of motor water-cooled systems.

Numerical methods

Thermal analysis

In this study, the temperature distribution of the drive motor and the flow pattern of the fluid were numerically calculated using the FEM, with water being used as the cooling fluid for the water-cooled system. By varying the cooling conditions and structural parameters of the water-cooled system, the temperature distribution of the motor under different cooling conditions is investigated and the heat transfer performance of the motor at different speeds is systematically tested. In the analysis, the dimensions of the 3-D finite element model are the same as the prototype. In order to simulate the real operation of the drive motor, good insulation of the motor is assumed. Other assumptions are:

– The fluid-flow velocity inside a water-cooled system is much less than the speed of sound, so the fluid is considered incompressible.
– The turbulence model is used to solve for the flow field due to the large Reynolds number of the fluid within the water-cooled system.
– The cooling fluid is assumed to enter the inlet of the water-cooled system at a vertical angle.

The heat transfer process in the EV drive motor is theoretically governed by the law of conservation of energy, the law of conservation of momentum and the law of conservation of mass. Of these, the law of conservation of energy is:

$$\frac{\partial(\rho T)}{\partial t}+\operatorname{div}(\rho \boldsymbol{u} T)=\operatorname{div}\left(\frac{k}{c_P}\operatorname{grad} T\right)+S_T \tag{1}$$

where c_p is the specific heat capacity, T – the temperature of the fluid, k – the heat transfer coefficient of the fluid, and S_T – the fluid heat source.

The law of conservation of momentum is:

$$\begin{aligned}
&\frac{\partial(\rho \boldsymbol{u})}{\partial t}+\operatorname{div}(\rho u u)=-\frac{\partial p}{\partial x}+\frac{\partial \tau_{xx}}{\partial x}+\frac{\partial \tau_{yx}}{\partial y}+\frac{\partial \tau_{zx}}{\partial z}+F_x\\
&\frac{\partial(\rho \boldsymbol{v})}{\partial t}+\operatorname{div}(\rho v u)=-\frac{\partial p}{\partial y}+\frac{\partial \tau_{xy}}{\partial x}+\frac{\partial \tau_{yy}}{\partial y}+\frac{\partial \tau_{zy}}{\partial z}+F_y\\
&\frac{\partial(\rho \boldsymbol{w})}{\partial t}+\operatorname{div}(\rho w u)=-\frac{\partial p}{\partial z}+\frac{\partial \tau_{xz}}{\partial x}+\frac{\partial \tau_{yz}}{\partial y}+\frac{\partial \tau_{zz}}{\partial z}+F_z
\end{aligned} \tag{2}$$

where i is the co-ordinate direction, F_i – the volume force on the microelement, p – the static pressure on the fluid microelement, and τ_{xx}, τ_{xy}, and τ_{xz} are the viscous stress components on the surface of the microelement.

The law of conservation of mass is:

$$\frac{\partial \rho}{\partial t}+\frac{\partial(\rho \boldsymbol{u})}{\partial x}+\frac{\partial(\rho \boldsymbol{v})}{\partial y}+\frac{\partial(\rho \boldsymbol{w})}{\partial z}=0 \tag{3}$$

where ρ is the fluid density, t – the time, and u, v, and w are the fluid velocity.

Considering the working condition of the drive motor during operation and taking into account the structural characteristics of the water-cooled system, the outer wall surface of the housing is considered as the boundary condition for natural convection. The other necessary boundary conditions are:

The inlet of the water-cooled system is defined as the velocity inlet and the outlet as the pressure outlet.

– The water temperature and flow rate at the inlet of the water-cooled system are maintained at 45 °C and 1.3 m/s, respectively, and subsequently change as the numerical simulation proceeds.
– Based on the actual operation of the water-cooled system, the outer wall surface of the rotor is defined as a rotating wall surface with an initial speed of 4000 rpm, which is subsequently changed as the numerical simulation proceeds.

The basic principles of fluid mechanics and heat transfer show that the flow and heat transfer of the cooling fluid in a PMSM for EV satisfy the laws of conservation of mass, momentum, and energy, and when the cooling fluid is incompressible and in a steady flow state, the control equations RNG and k-ε reflecting the turbulence characteristics should be used:

$$\frac{\partial}{\partial t}(\rho k)+\operatorname{div}(\rho k \boldsymbol{V})=\operatorname{div}\left[\left(\mu+\frac{\mu_t}{\sigma_k}\right)\operatorname{grad} k\right]+G_k-\rho \varepsilon \tag{4}$$

$$\frac{\partial}{\partial t}(\rho \varepsilon)+\operatorname{div}(\rho \varepsilon \boldsymbol{V})=\operatorname{div}\left[\left(\mu+\frac{\mu_t}{\sigma_\varepsilon}\right)\operatorname{grad} \varepsilon\right]+C_{1\varepsilon}\frac{\varepsilon}{k}G_k-C_{2\varepsilon}\rho\frac{\varepsilon^2}{k} \tag{5}$$

where k is the feature speed of turbulence kinetic energy, V – the fluid velocity vector, ε – the diffusion factor, α_k and α_ε are the reciprocals of the Prandtl number of equations k and ε, respectively, μ_t – the eddy viscosity coefficient, G_k – the turbulence generation rate, and $C_{1\varepsilon}$ and $C_{2\varepsilon}$ are the constants.

Field synergy analysis

The FSP can be illustrated here in terms of the boundary-layer problem of a laminar fluid-flowing through a 2-D flat plate. A fluid with flow velocity, U_∞, and temperature, T_h, flows horizontally through a horizontally placed flat plate with temperature T_p less than T_h. Let the thickness of the thermal boundary-layer be δ. Treating the convective term in the energy conservation equation for the laminar boundary-layer as a source term and integrating it yields:

$$\int_0^\delta \rho_f c_p\left(V_x\frac{\partial T}{\partial x}+V_y\frac{\partial T}{\partial y}\right)\mathrm{d}y=-\lambda_f\left.\frac{\partial T}{\partial y}\right|_w=q_w \tag{6}$$

where q_w is the heat flow density at the wall, λ_f – the thermal conductivity of the fluid, and ρ_f – the density of the fluid.

The left-hand side of the equal sign in eq. (6) is the sum of convective sources in the boundary-layer, while the right-hand side of the equal sign is the heat flow density at the wall. The traditional concept of source intensification assumes that the wall heat flow density is proportional to the sum of convective sources. However, when applying FSP to its analysis, the convective term of eq. (6) can be expressed in vector form as:

$$\int_0^{\delta} \rho_f c_p(\dot{\boldsymbol{U}})\mathrm{d}y = -\left.\frac{\partial T}{\partial y}\right|_w = q_w \tag{7}$$

where $\dot{\boldsymbol{U}}$ is the velocity vector of the fluid. Add the following dimensionless variables:

$$\bar{\boldsymbol{U}} = \frac{\dot{\boldsymbol{U}}}{\boldsymbol{U}_\infty},\quad \nabla\bar{T} = \frac{\nabla T\delta}{T_\infty - T_W},\quad \bar{y} = \frac{y}{\delta} \tag{8}$$

Taking eq. (8) into eq. (7) gives:

$$\mathrm{RePr}\int_0^1 \left(\bar{\boldsymbol{U}}\cdot\nabla\bar{T}\right)\mathrm{d}\bar{y} = \mathrm{Nu} \tag{9}$$

The factor being integrated in eq. (9) can be rewritten as:

$$\bar{\boldsymbol{U}}\cdot\nabla\bar{T} = \left|\bar{\boldsymbol{U}}\right|\cdot\left|\nabla\bar{T}\right|\cos\beta \tag{10}$$

where $\cos\beta$ is the cosine of the angle between the vector of the temperature gradient and the velocity vector, β also known as the synergy angle.

From eqs. (9) and (10), it can be shown that heat transfer can be enhanced by three methods:

– Increasing the Reynolds number, *e.g.* by increasing the flow rate to increase the degree of turbulence of the fluid.
– Increasing the Prandtl number, *e.g.* by using a cooling fluid with a higher specific heat capacity.
– Increasing the Nusselt number by reducing the synergy angle when the flow velocity as well as the temperature gradient are constant.

Proceeding from the aforementioned laminar flow boundary problem for a 2-D flat plate, we can also apply FSP to convective heat transfer in the water-cooled system of a drive motor, where the cosine of the angle between the temperature gradient field as well as the velocity field in the water-cooled system can be expressed as:

$$\cos\beta = \frac{\bar{\dot{U}}\cdot\nabla\bar{T}}{\left|\bar{\dot{U}}\right|\cdot\left|\nabla\bar{\dot{T}}\right|} \tag{11}$$

As the drive motor and its water-cooled system are modelled in 3-D in this study, the cosine value of the synergy angle can be further expressed as:

$$cos\beta = \frac{\frac{\partial T}{\partial x}V_x + \frac{\partial T}{\partial y}V_y + \frac{\partial T}{\partial z}V_z}{\sqrt{\left(\frac{\partial T}{\partial x}\right)^2 + \left(\frac{\partial T}{\partial y}\right)^2 + \left(\frac{\partial T}{\partial z}\right)^2}\sqrt{V_x^{\,2} + V_y^{\,2} + V_z^{\,2}}} \tag{12}$$

where $\partial T/\partial x$, $\partial T/\partial y$, and $\partial T/\partial z$ are the temperature gradients in the x-, y-, and z-directions, respectively, V_x, V_y, and V_z are the velocities in the x-, y-, and z-directions, respectively. The angle between the average velocity of the whole field and the temperature gradient can be expressed:

$$\beta_{WF} = \frac{\sum A_i B_i}{\sum A_i} \tag{13}$$

where A_i is the area of each control volume and β_i – the angle between the velocity and the temperature gradient at each node. The β_{WF} also known as the average synergy angle of the whole field (ASAWF). Alternatively, the field synergy number, *Fc*, can be used to evaluate the degree of field synergy in a drive motor water-cooled system:

$$Fc = \int \bar{U} \cdot \nabla \bar{T} \mathrm{d}\bar{y} = \frac{\mathrm{Nu}}{\mathrm{RePr}} \tag{14}$$

When the velocity field and temperature gradient field in the water-cooled system are in the same direction, Nu = RePr, *i.e. Fc* = 1, the convective heat exchange effect of the water-cooled system will reach its limit.

Physical model establishment

In this study, the EV drive motor with an axial water-cooled system is used as the research object and the basic parameters of the motor are given in tab. 1.

Table 1. Detailed parameters of the prototype motor

Parameter	Value	Parameter	Value
Rated power [kW]	40	Number of stator slots	36
Peak power [kW]	80	Number of poles	6
Rated rotational speed [rpm]	4000	Quantity of cooling channels (QCC)	8
Peak rotational speed [rpm]	9000	External diameter of stator [mm]	260

In order to obtain the steady-state temperature distribution of the motor and the fluid-flow pattern of the water-cooled system, the 3-D finite element model shown in fig. 1(a) was developed and solved in this study. Figure 1(b) shows the computational region of the water-cooled system with *QCC* = 8.

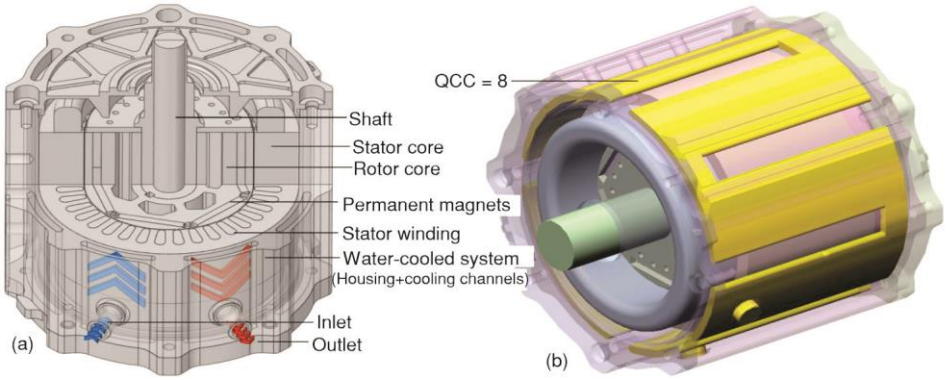

Figure 1. (a) 3-D finite element model and (b) water-cooled system calculation domain

Results and discussion

In order to analyze the synergy between the temperature gradient field and velocity field under different cooling conditions, and to investigate the influence of the inlet flow rate of the water-cooled system on the heat transfer performance of the EV drive motor, the inlet

flow rate range was set to 0.7-2.2 m/s, and the Reynolds number range was 2300 to 18570, in this range the cooling fluid was first in the transition phase from laminar to turbulent flow, followed by turbulent flow and its development. The temperature distribution and statistics of the drive motor windings for the different Reynolds number are shown in figs. 2 and 3, respectively.

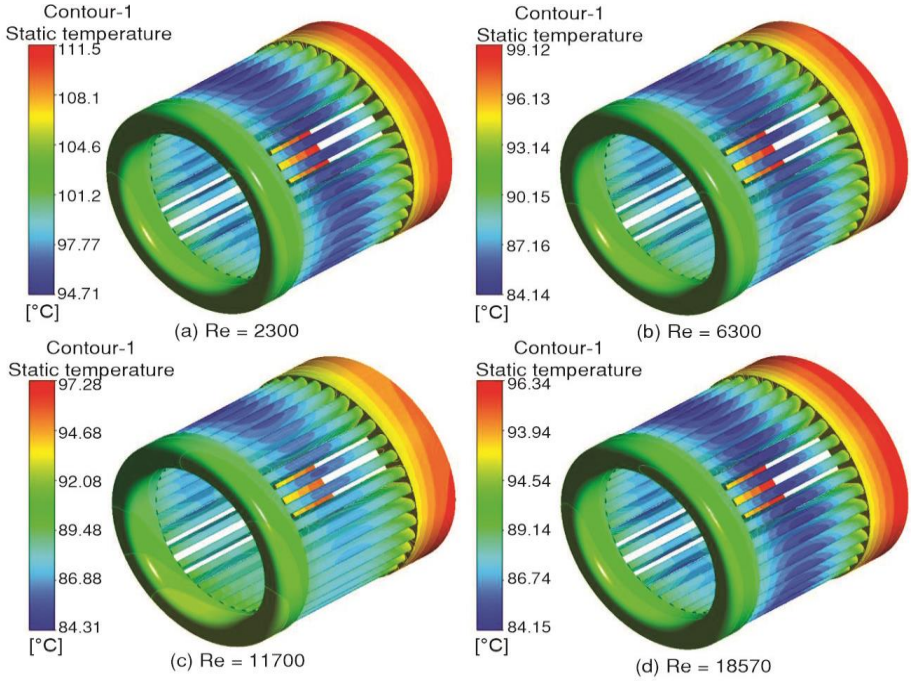

Figure 2. Temperature distribution of the drive motor windings with different Reynolds number; (a) Re = 2300, (b) Re = 6300, (c) Re = 11770, and (d) Re = 18570

As Reynolds number increases, the position of the high and low temperature areas of the winding does not change, the low temperature area is always located in the axial centre area, and the overall temperature distribution shows a trend of high at both ends and low at the centre. From a statistical viewpoint, when Reynolds number increases in the range of 2300 to 6300, the heat transfer efficiency of the cooling fluid per unit volume increases and the rate of decrease of the winding temperature is greater. In this interval, the maximum, average and minimum winding temperatures decrease at a rate of 11.18%, 10.39%, and 9.57%, respectively. However, it is worth noting that as Reynolds number continues to increase in the range 6300 to 18570, the decrease in winding temperature has slowed significantly: the maximum, average, and minimum winding temperatures decrease by 2.69%, 1.57%, and 1.02% respectively.

There are several reasons why we believe that the decreasing trend of winding temperature becomes slower. Firstly, by the time Reynolds number reaches around 6300, the bottom layer of the laminar flow is thin enough to weaken the effect of the thermal resistance of the water-cooled system on the heat transfer efficiency, which eventually makes the increasing trend of the cooling fluid heat transfer efficiency gradually slow down. Secondly, a clue can be found in the velocity vector distribution of the cooling fluid in fig. 4, as the maximum flow velocity is located near the bend of the cooling channels, implying that there is the wavy major

fluids with high vorticity. At the same time, there are vortexes with low vorticity at the front and back ends of the wavy major fluids, *i.e.* in the linear region of each of the cooling channels. As Reynolds number increases, the interaction between the vortexes and the wavy major fluids enhances, the vorticity of the wavy major fluids decreases and the scale of the vortexes increases, resulting in a decay of the turbulence kinetic energy, which ultimately inhibits the heat transfer efficiency of the cooling fluid.

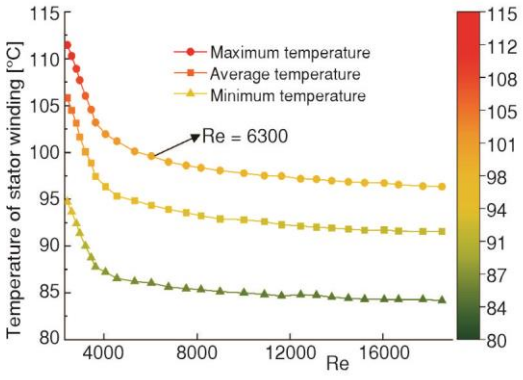

Figure 3. Statistics of winding temperature changes with Reynolds number

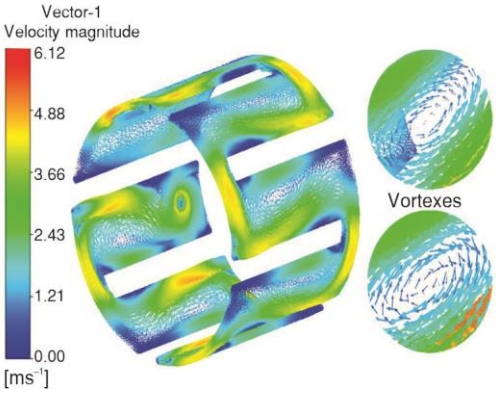

Figure 4. Speed vector of the cooling fluid during rated motor operation

In the previous description of the FSP we already know that the smaller the synergy angle and the larger the cosine of the angle between the velocity and temperature gradient fields, the higher the heat transfer efficiency for the same velocity and temperature boundary conditions. The relationship between the flow velocity and the motor temperature can also be interpreted and evaluated using the cosine of the synergy angle. The distribution of the cosine of the synergy angle as a changing of Reynolds number is shown in fig. 5.

The greater synergy (*i.e.* larger cosine values of the synergy angle) is mainly located at the bends of each cooling channel and at the wavy major fluids, due to the change in flow direction of the cooling fluid at the bends and the reduction in the cross-sectional area of the cooling channel, which forces the velocity vector of the cooling fluid to converge with the direction of the temperature gradient, further making the synergy angle rapidly decreases. The areas where the synergy is poor (*i.e.* where the cosine value is small) are mainly in the non-bending corners of each cooling channel and in the vortex areas, where the flow velocity is low and unevenly distributed, and where the fluid cannot flow outwards and stagnation and backflow are likely to occur, hence the poor synergy.

In addition, the computational hydrodynamics viewpoint also supports the above discussions on FSP. The viscous shear of the wall in the linear region of each cooling channel decreases the RMS of the flow velocity, while near the bend the velocity of the wavy major fluids increases the RMS of the flow velocity, resulting in a larger difference in the RMS of the flow velocity, which ultimately causes the overall velocity of cooling fluid at the bend to increase. In the range of Reynolds number from 2300 to 18750, vortexes with different vorticity are present in the cooling channels, and the fluid inside the vortexes is unable to flow outwards, this also laterally supports the viewpoint based on FSP. Similar to the trend of winding temperature with Reynolds number, the mean value of cosine is positively correlated with Reynolds

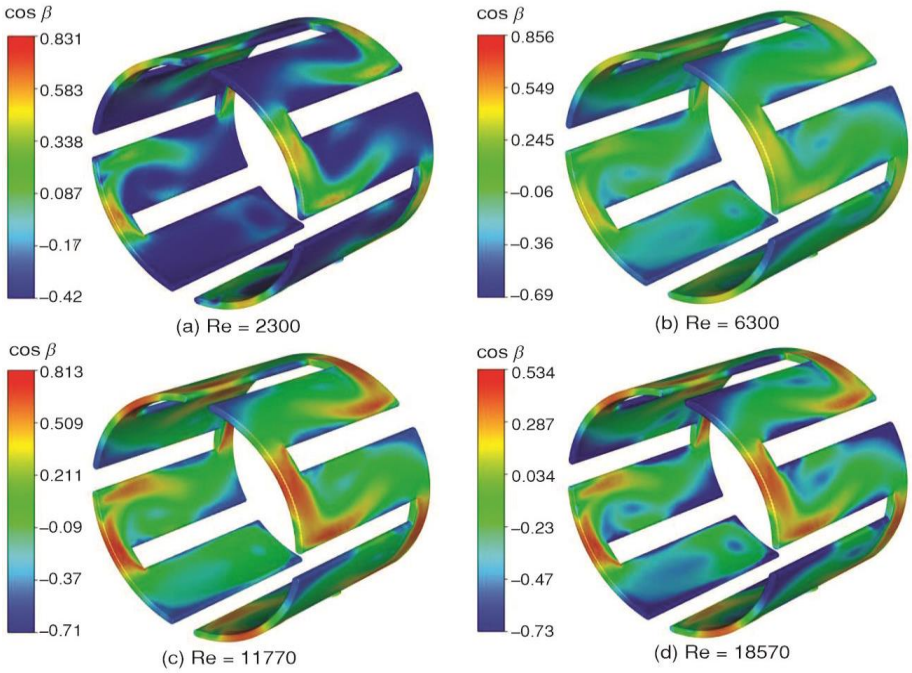

Figure 5. Distribution of the cosine of the synergy angle with Reynolds number; (a) Re = 2300, (b) Re = 6300, (c) Re = 11770, and (d) Re = 18570

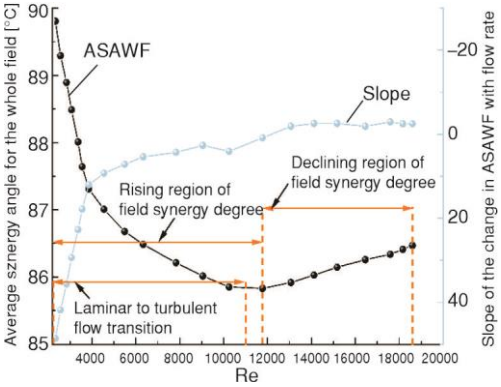

Figure 6. Variation of ASAWF with Reynolds number

number as Reynolds number increases in the interval from 2300 to 11770, with a gradual increase in synergy. However, when Reynolds number increases in the interval 11770 to 18570, the mean value of the cosine is negatively correlated with Reynolds number and the synergy gradually decreases. This phenomenon can be further argued from the perspective of the ASAWF, which and its slope with Reynolds number are shown in fig. 6.

When Reynolds number is at 2300 to 11030, the cooling fluid in the water-cooled system is in the transition process from laminar to turbulent flow and the ASAWF of the cooling fluid is constantly decreasing, but the rate of decrease is from fast to slow. *i.e.* The increase rate of the synergy angle's cosine value is also from fast to slow. As Reynolds number increases from 2300 to 11770, the ASAWF also decreases from 89.87° to 85.83°, a decrease of 4.49%, so the synergy between the velocity field and the temperature gradient field becomes stronger, but the trend of increasing synergy has completely slowed down at around Re = 11030.

It is worth noting that the heat transfer capacity of the water-cooled system reaches its peak when Reynolds number reaches around 11770, at the same time the increase in Reynolds number leads to an increase in ASAWF instead. When Re = 18570, ASAWF has already risen

to 86.47°, resulting in poor synergy and a decline in the heat transfer ability of the water-cooled system. The previous discussion is also supported by the trend of the slope, which changes from positive to negative around Re = 11770, which also proves that the heat transfer capacity of the water-cooled system has reached its limit as Reynolds number increases.

Figures 7(a) and 7(b) illustrate the relationship between stator winding temperature, permanent magnet temperature and QCC, respectively. As the QCC increases, the flow path and heat transfer area of the cooling fluid increases, and the temperature of the stator winding and permanent magnet shows a clear downward trend, and the maximum drop in temperature for both can reach 15.02 °C and 16.91 °C, respectively. Although the stator winding and permanent magnet temperatures are both decreasing, the decrease rate of the stator winding temperature is slightly higher than the decrease rate of the permanent magnet temperature, owing to the stator winding being closer to the water-cooled system in space than the permanent magnet.

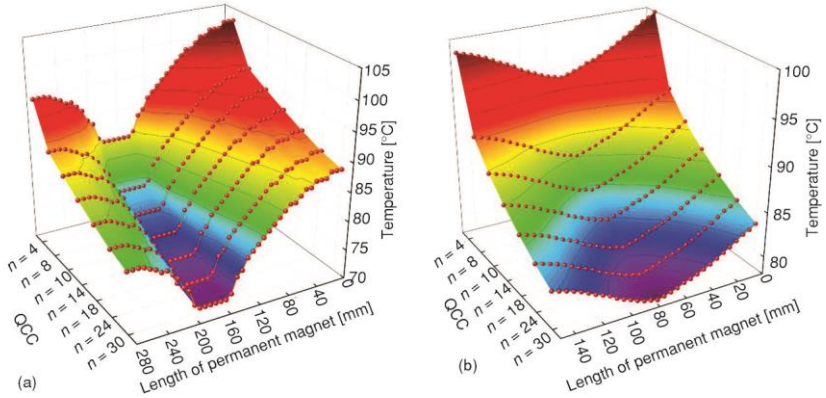

Figure 7. Relationship between; (a) stator winding temperature and QCC and (b) permanent magnet temperature and QCC

Figure 8(a) shows the relationship between the flow resistance of the water-cooled system and the QCC, while fig. 8(b) demonstrates the relationship between the Fc and QCC.

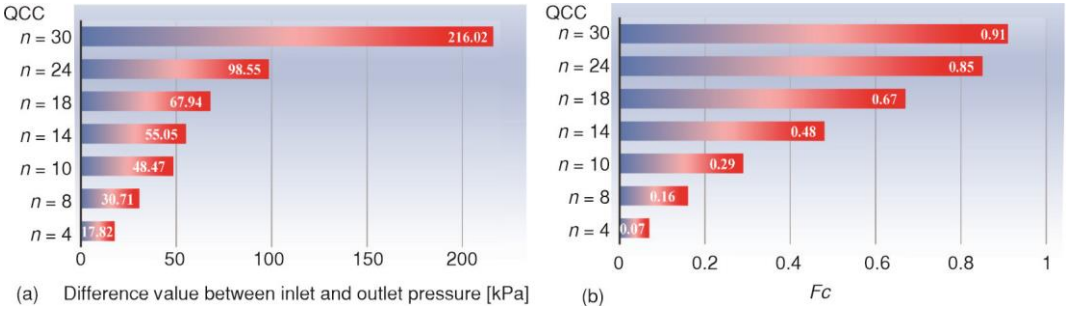

Figure 8. Relationship between; (a) the flow resistance of the water-cooled system and the QCC and (b) the *Fc* and QCC

Although QCC shows a clear positive correlation with *Fc*, especially when $QCC > 24$, *Fc* still maintains a growth rate of 7.06%. However, this requires the water-cooled system to provide a differential pressure of at least 98.55 kPa for the inlet and outlet, which also means that the growth rate of flow resistance in the water-cooled system starts to increase sharply when $QCC > 24$. Although the QCC is proportional to the heat transfer performance of the

water-cooled system, to balance the flow resistance with the QCC and also to avoid a blind increase in QCC, a more balanced and preferable scheme is to choose 18-24 for the QCC.

Experimental verification

To verify the accuracy of the theoretical analysis and simulation calculations, the EV drive motor was built with a rated power of 40 kW and equipped with the water-cooled system with $QCC = 8$. The temperature test platform and prototype of the drive motor are shown in fig. 9. The prototype on the test platform is controlled by torque and the accompanying motor is controlled by speed. To measure the winding temperature, thermocouples are placed on the inside of the winding end of the prototype.

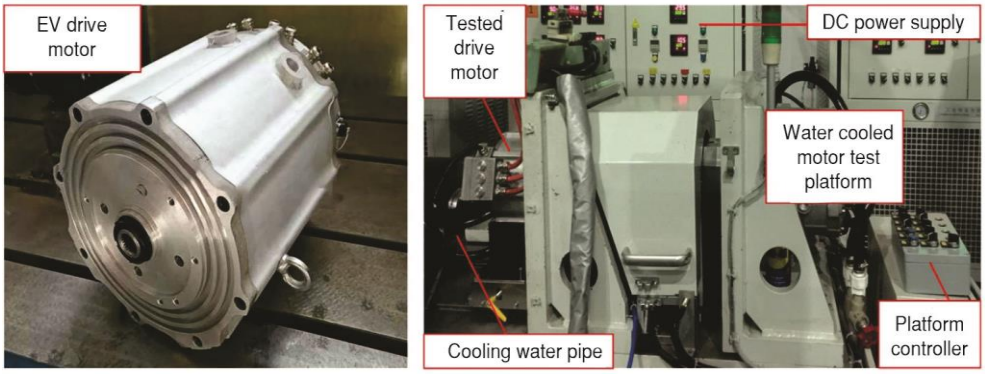

Figure 9. Drive motor (a) and experimental platform for temperature measurement (b)

To ensure the reasonability of the test, two working conditions were set up for the tested prototype: (1) 7000 rpm and 40 Nm and (2) 4000 rpm and 75 Nm. The test results are shown in fig. 10.

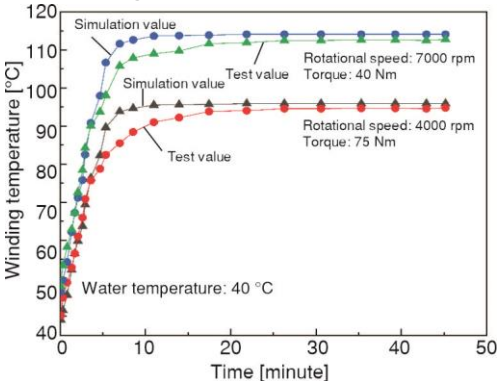

Figure 10. Comparison of test results with simulation results

From the sixth to the tenth minute of the test, the simulation results did not fit well with the test results. In particular, the working condition at 4000 rpm. This is due to the unstable residual values of the simulation caused by the setting of the boundary conditions, which further leads to a faster temperature growth rate in the early stages. In the later stages of the simulation, the error between the simulation results and the test results is further reduced, with the final error remaining at around 3%.

Conclusion

Thermal management of EV drive motors is a challenging design process and is often a key factor limiting motor performance improvement. Based on the FSP, this study has numerically evaluated and experimentally investigated the heat transfer performance of the drive motor water-cooled system and summarised the following key findings.

- Although Reynolds number is positively related to the heat transfer performance of the water-cooled system, the winding temperature does not decrease linearly with increasing

Reynolds number. As Reynolds number continues to increase in the interval from 6300 to 18570, the reduction of the winding temperature decrease narrows significantly, with a maximum difference of up to 8.82%. The variation of the Reynolds number growth interval and the positive evolution of the vortex are the two main reasons for the non-linear decrease in winding temperature.

- In water-cooled systems, the greater synergy areas are mainly located at the bends of each cooling channel and the wavy major fluids, while the lower synergy areas are mainly located at the non-bending corners of each cooling channel and the vortexes areas, which can also be explained by CFD.
- When Reynolds number is in the intervals 2300 to 11770 and 11770 to 18570, respectively, the synergy shows distinctly opposite trends. When the heat transfer capacity of the water-cooled system reaches its peak, the Reynolds number increases instead leading to the increase of the ASAWF, which ultimately causes a deterioration of the synergy between the velocity and temperature gradient fields.
- The QCC is positively correlated with *Fc*, and the maximum temperature of the stator winding and permanent magnets can be reduced by 14.58% and 16.92%, respectively by increasing the QCC. However, to balance the QCC with the flow resistance, the QCC selection of n = 18-24 is the preferred and more balanced solution.

References

[1] Tang, H., *et al*., Review of Applications and Developments of Ultra-Thin Micro Heat Pipes for Electronic Cooling, *Applied Energy*, *223* (2018), Aug., pp. 383-400
[2] Xu, L., *et al*., Comparative Analysis and Design of Partitioned Stator Hybrid Excitation Axial Flux Switching PM Motors for In-Wheel Traction Applications, *IEEE Transactions on Energy Conversion*, *37* (2022), 2, pp. 1416-1427
[3] Habib, K., *et al*., Exploring Rare Earths Supply Constraints for the Emerging Clean Energy Technologies and the Role of Recycling, *Journal of Cleaner Production*, *84* (2014), 3, pp. 348-359
[4] Haidar, A. M. A., *et al*., Technical Challenges for Electric Power Industries due to Grid-Integrated Electric Vehicles in Low Voltage Distributions: A Review, *Energy Conversion and Management*, *86* (2014), Oct, pp. 689-700
[5] Yu, W., *et al*., Coupled Magnetic Field-Thermal Network Analysis of Modular-Spoke-Type Permanent-Magnet Machine for Electric Motorcycle, *IEEE Transactions on Energy Conversion*, *36* (2020), 1, pp. 120-130
[6] Wang, J. X., *et al*., Experimental Investigation of the Thermal Control Effects of Phase Change Material Based Packaging Strategy for On-Board Permanent Magnet Synchronous Motors, *Energy Conversion and Management*, *123* (2016), 5, pp. 232-242
[7] Qi, J., *et al*., Thermal Analysis of Modular-Spoke-Type Permanent-Magnet Machines Based on Thermal Network and FEA Method, *IEEE Transactions on Magnetics*, *55* (2019), 7, pp. 1-5
[8] Kampker, A., *et al*., Technological and Total Cost of Ownership Analysis of Electric Powertrain Concepts for Long-Haul Transport in Comparison to Traditional Powertrain Concepts, *Proceedings*, 8th International Electric Drives Production Conference, Schweinfurt, Germany, 2018, pp. 1-7
[9] Chin, J. W., *et al*., High Efficiency PMSM with High Slot Fill Factor Coil for Heavy-Duty EV Traction Considering AC Resistance, *IEEE Transactions on Energy Conversion*, *36* (2020), 2, pp. 883-894
[10] Giangrande, P., *et al*., Considerations on the Development of an Electric Drive for a Secondary Flight Control Electromechanical Actuator, *IEEE Transactions on Industry Applications*, *55* (2019), 4, pp. 3544-3554
[11] Bramerdorfer, G., *et al*., Modern Electrical Machine Design Optimization: Techniques, Trends, and Best Practices, *IEEE Transactions on Industrial Electronics*, *65* (2018), 10, pp. 7672-7684
[12] Kang, M., *et al*., Self-Circulation Cooling Structure Design of Permanent Magnet Machines for Electric Vehicle, *Applied thermal engineering*, *165* (2020), 114593
[13] Petrov, I., *et al*., Investigation of a Direct Liquid Cooling System in a Permanent Magnet Synchronous Machine, *IEEE Transactions on Energy Conversion*, *35* (2019), 2, pp. 808-817

[14] Du, G., *et al*., Power Loss and Thermal Analysis for High-Power High-Speed Permanent Magnet Machines, *IEEE Transactions on Industrial Electronics, 67* (2020), 4, pp. 2722-2733
[15] Chang, J., *et al*., A Yokeless and Segmented Armature Axial Flux Machine with Novel Cooling System for In-Wheel Traction Applications, *IEEE Transactions on Industrial Electronics, 68* (2021), 5, pp. 4131-4140
[16] Gai, Y., *et al*., Numerical and Experimental Calculation of CHTC in an Oil-Based Shaft Cooling System for a High-Speed High-Power PMSM, *IEEE Transactions on Industrial Electronics, 67* (2020), 6, pp. 4371-4380
[17] Lindh, P., *et al*., Direct Liquid Cooling Method Verified with an Axial-Flux Permanent-Magnet Traction Machine Prototype, *IEEE Transactions on Industrial Electronics, 64* (2017), 8, pp. 6086-6095
[18] Guo, Z. Y., *et al*., A Novel Concept for Convective Heat Transfer Enhancement, *International Journal of Heat and Mass Transfer, 41* (1998), 14, pp. 2221-2225
[19] Gu., Z. Y., *et al*., Mechanism and Control of Convective Heat Transfer-Coordination of Velocity and Heat Flow Fields, *Chinese Science Bulletin, 46* (2001), Apr., pp. 596-599
[20] Guo, Z. Y., *et al*., The Field Synergy (Coordination) Principle and Its Applications in Enhancing Single Phase Convective Heat Transfer, *International Journal of Heat and Mass Transfer, 48* (2005), 9, pp. 1797-1807
[21] Chen, Q., *et al*., Field Synergy Equation for Turbulent Heat Transfer and Its Application, *International Journal of Heat and Mass Transfer, 50* (2007), 25, pp. 5334-5339
[22] Tao, W. Q., *et al*., Field Synergy Principle for Enhancing Convective Heat Transfer – Its Extension and Numerical Verifications, *International Journal of Heat and Mass Transfer, 45* (2002), 18, pp. 3849-3856
[23] Tao, W. Q., *et al*., A Unified Analysis on Enhancing Single Phase Convective Heat Transfer with Field Synergy Principle, *International Journal of Heat and Mass Transfer, 45* (2002), 24, pp. 4871-4879
[24] Ma, L. D., *et al*., Experimental Verification of the Field Synergy Principle, *International Communications in Heat and Mass Transfer, 34* (2007), 3, pp. 269-276
[25] Liu, W., *et al*., Physical Quantity Synergy in Laminar Flow Field of Convective Heat Transfer and Analysis of Heat Transfer Enhancement, *Chinese Science Bulletin, 54* (2009), Oct., pp. 3579-3586
[26] Liu, W., *et al*., Physical Quantity Synergy in the Field of Turbulent Heat Transfer and Its Analysis for Heat Transfer Enhancement, *Chinese Science Bulletin, 55* (2010), Aug., pp. 2589-2597
[27] Fu, Y., *et al*., Analysis on the Convective Heat Transfer in a Rotating Tube with Field Synergy Principle, *Proceedings of the CSEE, 28* (2008), 17, pp. 70-75

Paper submitted: April 22, 2023
Paper revised: June 28, 2023
Paper accepted: July 3, 2023